



HAL
open science

Depth Constraints on Coseismic Velocity Changes From Frequency Dependent Measurements of Repeating Earthquake Waveforms

Yixiao Sheng, William L. Ellsworth, Ariel Lellouch, Gregory C. Beroza

► **To cite this version:**

Yixiao Sheng, William L. Ellsworth, Ariel Lellouch, Gregory C. Beroza. Depth Constraints on Coseismic Velocity Changes From Frequency Dependent Measurements of Repeating Earthquake Waveforms. *Journal of Geophysical Research: Solid Earth*, 2021, 126, pp.1053-1064. 10.1029/2020JB020421 . insu-03594415

HAL Id: insu-03594415

<https://insu.hal.science/insu-03594415>

Submitted on 23 Jun 2022

HAL is a multi-disciplinary open access archive for the deposit and dissemination of scientific research documents, whether they are published or not. The documents may come from teaching and research institutions in France or abroad, or from public or private research centers.

L'archive ouverte pluridisciplinaire **HAL**, est destinée au dépôt et à la diffusion de documents scientifiques de niveau recherche, publiés ou non, émanant des établissements d'enseignement et de recherche français ou étrangers, des laboratoires publics ou privés.

Copyright

JGR Solid Earth

RESEARCH ARTICLE

10.1029/2020JB020421

Key Points:

- We estimate velocity change from the coda of repeating earthquakes and find larger change of low-frequency coda than high-frequency coda
- Downhole geophones and distributed acoustic sensing records confirm that near-surface reverberations dominate low-frequency coda waves
- The frequency dependence of seismic velocity change suggests it is an effect of the shallow crust

Supporting Information:

- Supporting Information S1
- Table S1

Correspondence to:

Y. Sheng,
yixiao.sheng@univ-grenoble-alpes.fr

Citation:

Sheng, Y., Ellsworth, W. L., Lellouch, A., & Beroza, G. C. (2021). Depth constraints on coseismic velocity changes from frequency-dependent measurements of repeating earthquake waveforms. *Journal of Geophysical Research: Solid Earth*, 126, e2020JB020421. <https://doi.org/10.1029/2020JB020421>

Received 16 JUN 2020
 Accepted 5 JAN 2021

Depth Constraints on Coseismic Velocity Changes From Frequency-Dependent Measurements of Repeating Earthquake Waveforms

Yixiao Sheng^{1,2} , William L. Ellsworth¹ , Ariel Lellouch¹ , and Gregory C. Beroza¹ 

¹Department of Geophysics, Stanford University, Stanford, CA, USA, ²Institut des Sciences de la Terre, Université Grenoble Alpes, CNRS, Grenoble, France

Abstract We revisit velocity changes caused by the 2004 Parkfield earthquake through the analysis of the coda of repeating earthquakes. Our results reveal the change to be strongly frequency dependent. Low-frequency components of the coda of repeating earthquakes are more affected by the velocity alteration than high-frequency components. We interpret this to indicate that the coseismic velocity reduction primarily occurs at a shallow depth, and is expressed in low-frequency energy resulting from reverberations near the Earth's surface. This can only be observed at low frequencies because the shallow crust is highly dissipative. The high-frequency component is relatively unaffected, as it is comprised of body waves scattered throughout the crust. We support this argument with direct observations of seismic wavefields across a wide range of depths in the shallow crust, supplemented by using downhole geophones and distributed acoustic sensing measurements.

Plain Language Summary Seismic velocity reduction in the crust triggered by large earthquakes has been widely observed, yet the mechanism remains controversial. Central to the disagreement is the depth of the velocity change. In this study, we investigate the seismic velocity change associated with the 2004 Mw 6.0 Parkfield earthquake. We provide new evidence to support the argument that the velocity alteration caused by this large earthquake is dominated by changes at shallow depth.

1. Introduction

Passive monitoring for time-dependent seismic velocity using seismic interferometry has seen increasing application. Research targets range from monitoring fault systems (e.g., Brenguier, Campillo, et al., 2008; Hadziioannou et al., 2011; Wu et al., 2016) to forecasting volcanic intrusions (e.g., Brenguier, Shapiro, et al., 2008; Sens-Schönfelder & Wegler, 2006; Obermann, Planès, Larose, & Campillo, 2013), to probing changes in shallow groundwater (Clements & Denolle, 2018). The interpretation of these results assumes that the cross-correlation coda of seismic noise travels over a longer path that more broadly samples the medium than the direct waves. Localizing the velocity perturbations in a 3D space is essential to interpreting their origin and has seen some progress (e.g., Obermann et al., 2019; Obermann, Planès, Larose, Sens-Schönfelder, et al., 2013); however, it remains challenging due to uncertainties in the composition of the correlation coda. This is particularly true for the later coda. Obermann, Planès, Larose, Sens-Schönfelder, et al. (2013) proposed that the early part of the correlation coda is dominated by surface waves while the later part is dominated by body waves. Wu et al. (2016) disagreed and claimed the entire coda is composed of surface waves with the argument that the frequency-dependent velocity change they observed at Parkfield originates from surface-wave dispersion. Sheng et al. (2018) further pointed out that coda waves are modulated by the original noise source distribution, if there is insufficient ensemble averaging. Understanding the composition of the coda of the cross-correlation function is crucial because it determines the choice of the proper kernel for locating and interpreting the source of the observed velocity changes. Before noise correlations, there was a long history of using repeating earthquakes to investigate velocity perturbations (e.g., Peng & Ben-Zion, 2006; Poupinet et al., 1984; Rubinstein & Beroza, 2005; Schaff & Beroza, 2004). Because repeating events are associated with creeping faults and have low temporal resolution due to long interevent times, their application is limited. When available, however, repeating earthquakes provide independent constraints on changes in structure. A better understanding of the coda of repeating earthquakes has the potential to improve the understanding of the coda of cross-correlations.

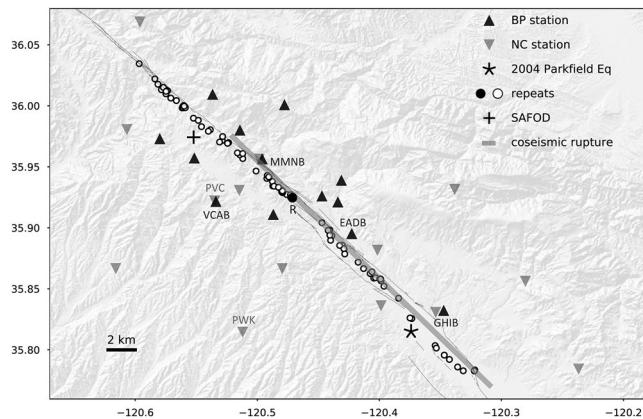


Figure 1. Reference map of the study area showing HRSN borehole stations (BP), Northern California seismic network (NCSN) surface stations (NC), the SAFOD borehole, the 2004 Parkfield earthquake epicenter, the surface projection of the coseismic rupture zone (Murray & Langbein, 2006), and the locations of repeating earthquakes used in this study. Among these repeating earthquakes, the solid circle highlights the representative event-pair that listed in Table 1. HRSN, high-resolution seismic network; SAFOD, San Andreas fault observatory at depth.

Velocity changes associated with large earthquakes have been observed repeatedly; however, there remains differing interpretations about whether the change is due to the material damage within the superficial layers caused by the strong shaking (e.g., Dodge & Beroza, 1997; Rubinstein & Beroza, 2005; Schaff & Beroza, 2004; Sleep, 2009; Wu et al., 2016) or arises from deformation at greater depth (e.g., Brenguier, Shapiro, et al., 2008; Froment et al., 2013; Obermann, Planès, Larose, Sens-Schönfelder, et al., 2013). In this study, we revisit the velocity change near Parkfield due to the 2004 Mw 6.0 Parkfield earthquake. We focus on the analysis of repeating earthquakes, and particularly on the coda of S waves. We observe that low-frequency energy gradually comes to dominate the coda, suggesting strong attenuation of the high-frequency content. We report new observations that reveal a frequency-dependent response of earthquake coda to seismic velocity perturbation, and find that low-frequency (1–5 Hz) signals are more strongly affected by the velocity changes than their high-frequency (10–20 Hz) counterparts. We also present new evidence from seismic recordings at the San Andreas Fault Observatory at Depth (SAFOD), revealing strong low-frequency reverberations near the Earth's surface, especially in the top 200 m. These seismic recordings are from dense downhole seismic arrays, which provide high-resolution spatial samplings of the seismic wavefields. We further perform coda wave interferometry between two collocated stations, one in the borehole and another on the surface. The resulting correlation functions confirm the

existence of the near-surface reverberations. All these observations together suggest that S-wave coda is dominated by long-period vibrations, and that the low-frequency character of the velocity change arises because these waves are trapped in the shallow sedimentary layers of the uppermost crust where velocity changes are concentrated.

2. Data

We first implement template matching using the FMF package (Beaucé et al., 2018) on earthquakes documented in the Double-Difference (Waldhauser, 2009) catalog provided by the Northern California Earthquake Data Center. We use the high-resolution seismic network (HRSN) borehole stations for this task and the seismograms are bandpass-filtered between 3 and 12 Hz. The templates are 8 s long and start 1 s before the P-wave arrival on each vertical component and 2 s before the S-wave arrival on horizontal components. The detection threshold is 0.92 for the average cross-correlation coefficient. We detect 88 repeating families containing earthquakes during the years 2003–2005. A total of 48 of these families have event-pairs that span the 2004 Parkfield earthquake, denoted as type A event-pairs, and the other 40 families only have earthquakes that occurred after the mainshock, marked as type B. The complete earthquake list is given in Table S1. We use PhaseNet (Zhu & Beroza, 2018), a neural network-based phase picker, to time the arrivals of both P- and S-waves. The picked phases, along with cross-correlation based travel-time differences are used as input to HypoDD (Waldhauser, 2001) to relocate the events and confirm that they are true repeats. As shown in Figure 1, these repeating earthquakes are well-distributed along the San Andreas Fault. Therefore, our analysis should reflect a general behavior of seismic velocity change in response to the 2004 Parkfield earthquake rather than the behavior along a particular source-receiver path. To illustrate our method in the following section, we present the results from one type B event-pair, denoted as R and marked by a solid circle in Figure 1. The details of this representative repeat are listed in Table 1. Note that a type B event-pair comprises two earthquakes that occurred after the mainshock and the resolved time shift samples the postseismic velocity recovery; while a type A event-pair spans the mainshock so that the associated time shift reflects the coseismic velocity reduction. We report our analysis of the vertical component only throughout the manuscript.

| Event group | Date | Time | Latitude | Longitude | Depth | Mag (M_d) |
|-------------|--------------------|-------------|-----------|-------------|-------|---------------|
| R | September 29, 2004 | 09:33:02.52 | 35.923792 | -120.470435 | 5.112 | 1.28 |
| | October 5, 2004 | 21:28:22.19 | 35.923800 | -120.470451 | 5.106 | 1.21 |

3. Relative Time Shift

Under the assumption of a spatially homogeneous velocity change, for repeated signals, the velocity perturbation dV is related to the coda wave arrival time difference dt as:

$$\frac{dV}{V} = -\frac{dt}{t} \quad (1)$$

where t is the lapse time in the coda and V is the background velocity before the perturbation occurs. After measuring the time shift between waveforms of repeating earthquakes, we can estimate dt/t , and obtain the relative velocity change dV/V . We use dynamic time warping (DTW) to extract that time shift $dt(t)$. DTW is a widely used algorithm for measuring the similarity between two time series. It finds the optimal alignment that minimizes a predefined distance metric. Hale (2013) and Mikesell et al. (2015) provide a detailed description of DTW so we only list the major steps. Given two time series $u(t)$ and $v(t)$, we first calculate an error vector at each time step t_i (assuming n time steps in total):

$$e(t_i, \tau) = (u(t_i) - v(t_i + \tau))^2 \quad \tau \in (-\tau_{max}, \tau_{max}) \quad (2)$$

where τ_{max} defines the range of points on $v(t)$ that any point on $u(t)$ is compared with. τ_{max} should be carefully chosen given prior information to save computation time and we use 0.2 s in our analysis based on previous studies on the velocity change in the area (e.g., Hadziioannou et al., 2011; Wu et al., 2016). Note that in Equation 2, the error is defined as the L2 norm of the difference between $u(t)$ and $v(t + \tau)$. Other forms can also be applied, such as the absolute value of the difference. The second step is accumulating the errors in time through a distance function:

$$d(t_1, \tau) = e(t_1, \tau) \quad (3)$$

$$d(t_i, \tau_j) = e(t_i, \tau_j) + \min \begin{cases} d(t_{i-1}, \tau_{j-1}) \\ d(t_{i-1}, \tau_j) \\ d(t_{i-1}, \tau_{j+1}) \end{cases} \quad (4)$$

In the distance matrix \mathbf{d} each path connecting t_1 and t_n represents one possible alignment between $u(t)$ and $v(t)$. By finding the path that gives the minimum accumulated misfit, we obtain the most favorable alignment, which yields the time shift at each time step considered. Mikesell et al. (2015) compared different techniques used for measuring phase shifts and concluded that DTW is less susceptible to cycle skipping given low signal-to-noise ratio (SNR), and that it yields better time resolution in detecting changes when the effect of the velocity perturbation is localized in the time series. Figure 2 shows a comparison between the commonly used moving-window cross-spectral (MWCS) method (Poupinet et al., 1984) and the DTW method in resolving the time shift between the events in the representative repeats R recorded at station BP.EADB (network.station). The window length used in MWCS is 2.5 s with a step of 0.25 s. The middle two panels show the target seismograms and the first

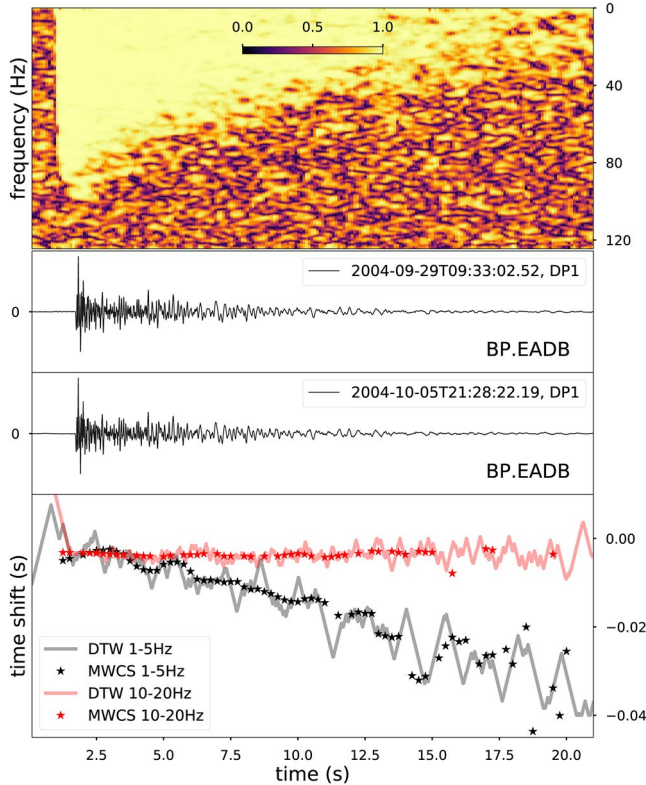


Figure 2. Comparison between the DTW and MWCS methods. The middle two panels show the waveforms of the two repeating earthquakes recorded on station EADB in the BP network. The first panel shows the cross-coherence of the waveforms as a function of frequency and time. The bottom panel illustrates the extracted time shift, using the DTW and MWCS methods for two distinct frequency bands. DTW, dynamic time warping; MWCS, moving-window cross-spectral.

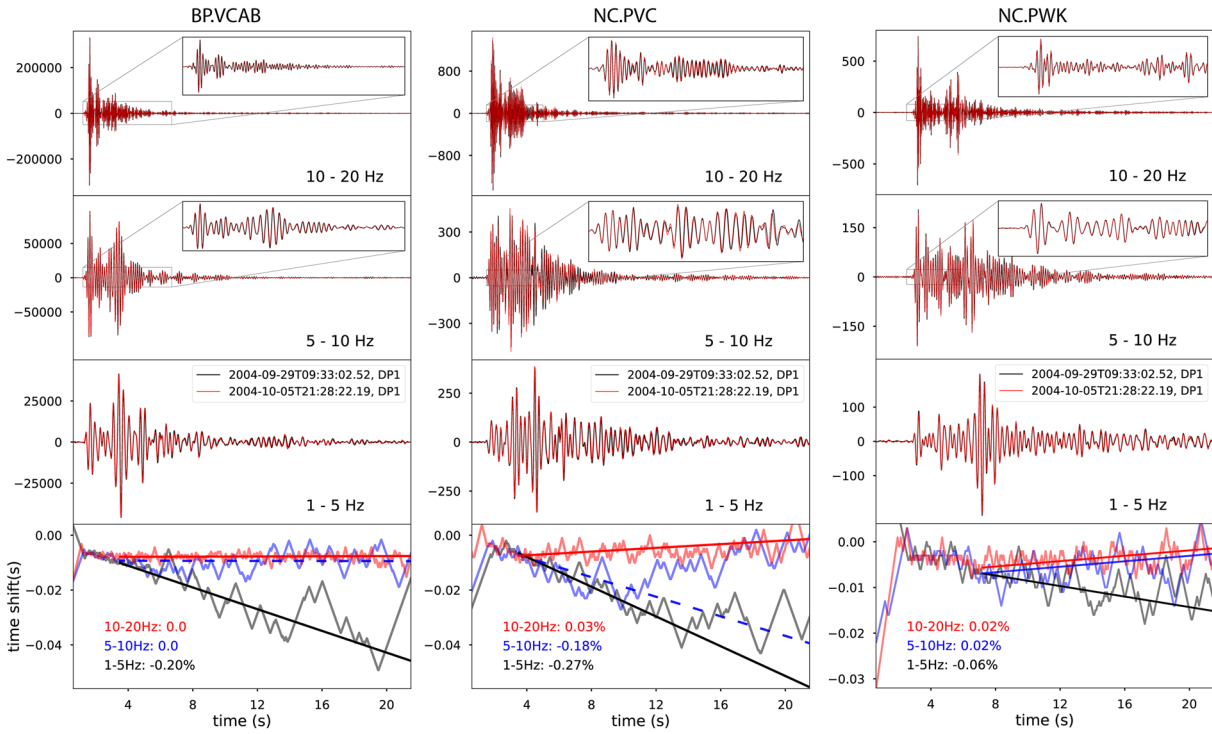


Figure 3. Examples of the frequency-dependent time shift estimated from repeating earthquakes. From left to right, the panels show the results for three different stations, VCAB in the BP network, PVC and PWK in the NC network. The relative time shift dt/t is listed in each panel.

panel shows the cross-coherence as a function of time and frequency. For a segment of $u(t)$ and $v(t)$ starting at time τ , the corresponding cross-coherence is defined as:

$$C_{uv}(\tau, f) = \frac{|S_{uv}(\tau, f)|}{\sqrt{S_{uu}(\tau, f)S_{vv}(\tau, f)}} \quad (5)$$

where $S_{uv}(\tau, f)$ is the cross-spectral density, and $S_{uu}(\tau, f)$ and $S_{vv}(\tau, f)$ the autospectral density of u and v , respectively. The absence of high-frequency signals in the late coda and the rapid decay of cross-coherence at high frequencies (higher than 40 Hz) indicate the strong scattering and attenuation in the study area. In the two target frequency bands, 1–5 Hz and 10–20 Hz, a drop in the waveform coherence starts around 15 s, after which we observe large fluctuations in the resolved time shifts. However, DTW is less affected by the decreasing SNR. As mentioned earlier, both of the repeating earthquakes in the representative event-pair happened after the 2004 Parkfield earthquake and therefore the estimated time shift has a negative trend, indicating postseismic velocity increase (recovery). The time-shift measurements from both methods agree with each other. In particular, the MWCS time shift appears to be a sparse and smoothed version of the DTW result. Interestingly, a noticeable difference between the two frequency bands appears following the S-wave arrival.

To illustrate that the frequency-dependent velocity change is a general phenomenon, we present the time shift estimates at three more stations in Figure 3 from the same pair of repeating earthquakes. In these examples, stations BP.VCAB and NC.PVC are co-located, with the former deployed in the borehole (around 200 m deep) and the latter on the Earth's surface, as is the third station NC.PWK. All of these stations are located outside of the fault zone, as shown in Figure 1. The waveforms are each bandpass-filtered at three different frequency bands for the time-shift measurements. We follow Equation 1 and estimate dt/t on the S-wave coda to quantify the relative velocity change. Note that the assumption of homogeneous velocity change is implied in Equation 1, but is not required by the DTW method. dt/t is calculated through a weighted linear regression using the average waveform cross-coherence in the targeted frequency band as the weight. Figure S1 shows a map view of dt/t from the same event-pair. Our results demonstrate that coda

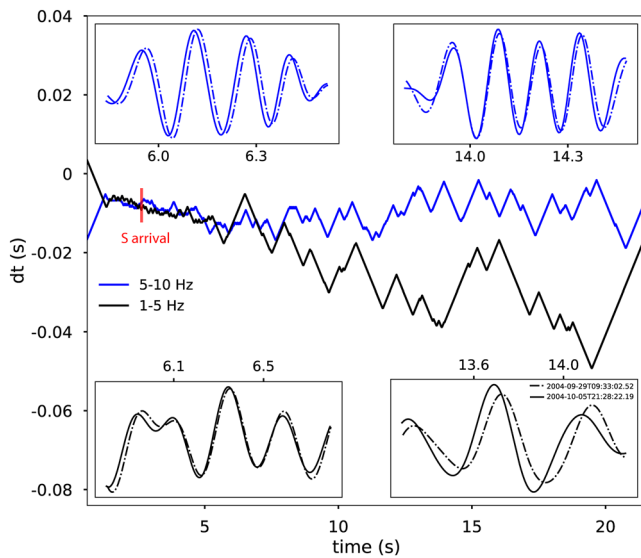


Figure 4. Time shift estimated on station BP.VCAB in the 1–5 Hz and 5–10 Hz frequency bands. The results exhibit an agreement in the early coda but clear discrepancy afterward. The four insets show segments of the coda wave, 5–10 Hz in blue and 1–5 Hz in black.

waves in the 10–20 Hz frequency bands are insensitive to the velocity change, while 1–5 Hz coda waves exhibit significant velocity variation. This observation is consistent over all stations, whether they are located at the Earth’s surface or in a borehole. The farther the station is away from the fault zone, the smaller the observed velocity variation, indicating the velocity change is not spatially homogeneous and broadly peaks around the fault. It is worth noting that on station NC.PVC in the 5–10 Hz frequency band, $dt(t)$ first increases along the early coda, following the same trend in the 1–5 Hz frequency band but then rolls back, falling toward a level comparable to the time shift at 10–20 Hz on the late coda. Such a phenomenon is also observed on station BP.VCAB but less obvious. Figure 4 further illustrates this point by showing the estimated time shifts on BP.VCAB accompanied with the waveforms of both early and late coda. The travel-time differences revealed on the waveforms clearly reflect the trend of time shift in each frequency band. Figure S2 provides more examples to support that such a time-shift rollback is not exceptional. We discuss the possible explanation in the later part of this manuscript. Due to the nonmonotonic time shift at 5–10 Hz, which is not suitable for estimating dV/V through Equation 1, we focus on the analysis of the other two frequency bands in the following section.

4. Continuous Velocity Variation

We apply the same analysis on all pairs of repeating earthquakes in both 1–5 Hz and 10–20 Hz frequency bands. Figure 5 displays histograms of the estimated relative time shifts. We note that the number of measurements from type A event-pairs is smaller than the number from type B, even though more type A event-pairs are detected. This is because many type A event-pairs contain earthquakes with relatively small magnitudes, resulting in waveforms with SNR that are too low for reliable measurements. We discard a waveform pair if the average cross-coherence (1–20 Hz) is smaller than 0.9. dt/t varies in a large range at low frequencies but centers around zero at high frequencies.

Such a data set with rich sampling of both velocity reduction and recovery provides an opportunity to resolve the temporal behavior of velocity perturbations. Following previous studies (e.g., Beroza et al., 1995; Hotovec-Ellis et al., 2014; Schaff & Beroza, 2004), we use a linear least squares inversion to estimate the velocity perturbation as a function of time after the mainshock. We first map the measured relative time shift dt/t to relative velocity change dV/V using Equation 1. For any pair of earthquakes that occurred at time t_i and t_j recorded at station sta , we can write the forward problem as:

we can write the forward problem as:

$$\frac{dV}{V}(t_i, t_j, sta) = \mu(t_j, sta) - \mu(t_i, sta) \quad (6)$$

where $\mu(t, sta)$ is the continuous velocity change that varies with seismic stations. We do not expect that the seismic velocity drop is spatially homogeneous, but incorporating all repeats into the inversion implies for each station, we aim to solve for an average velocity-change response. To set up the inverse problem, we exclude samples that do not match the event-pair type, that is, positive dV/V for type A event-pair or negative dV/V for type B event-pair. A complicating factor is the 2003 San Simeon earthquake of December 22, which also caused a velocity perturbation at Parkfield (Brennguier, et al., 2008a; Hadziioannou et al., 2011; Wu et al., 2016). For this reason, we exclude the event-pairs with earthquakes that happened in 2003 and make the approximation of no velocity change before the 2004 Parkfield earthquake, which is a reasonable approximation since the effect of the San Simeon earthquake was a small fraction of the effect

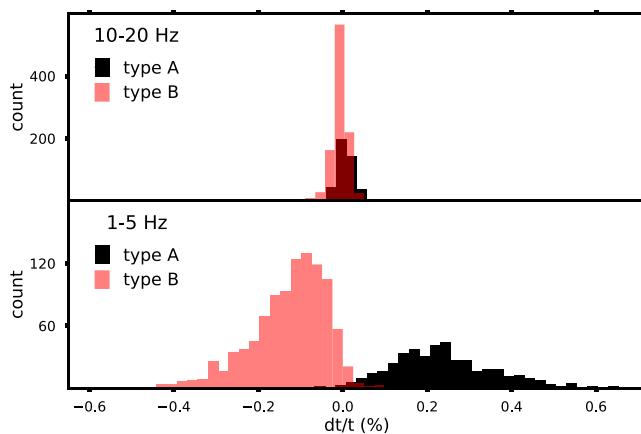


Figure 5. Histograms of estimated dt/t from all the available repeats and seismic stations. The results from different types of event-pairs are color coded. Type A event-pairs span the 2004 Parkfield Earthquake while both type B earthquakes are postmainshock.

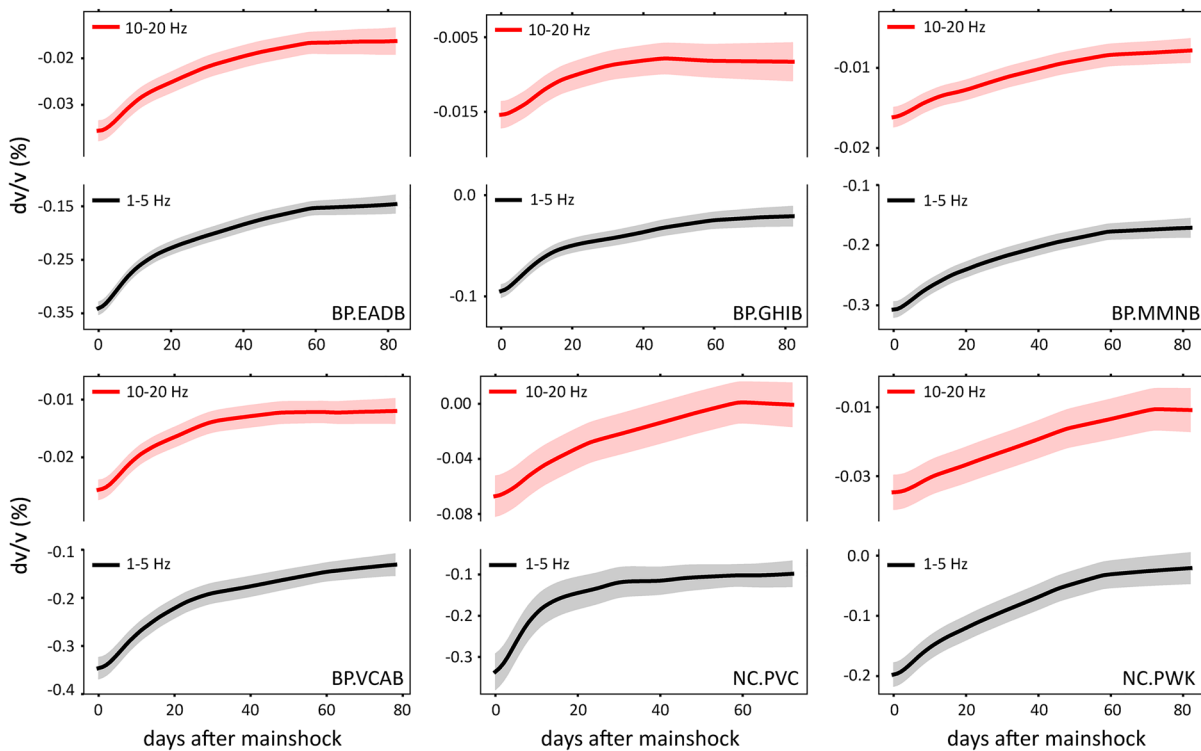


Figure 6. Examples of resolved continuous velocity change after the 2004 Parkfield earthquake. Different panels show the solutions for different stations with locations indicated in Figure 1. The light color area in each panel highlights the standard error.

of the Parkfield earthquake ($\sim 10\%$ reported in Wu et al., 2016). We then discretize $\mu(t, sta)$ evenly in time with a spacing of one day and interpolate the dV/V to a regular time grid. We add a Tikhonov regularization that minimizes the first-order time derivative of the solution. The regularization parameter is chosen after cross validation following Matthews and Segall (1993). For each station, we perform inversion in both frequency bands. Representative results are shown in Figure 6 and the rest are shown in Figures S3 and S4. Figure 7 shows the resolved coseismic velocity drop as a function of the peak ground velocity (PGV) of the 2004 Parkfield mainshock. Following Rubinstein and Beroza (2005), we estimate PGV at each station (Figure S5) through spatial interpolation of ShakeMap (Boatwright et al., 2003). Because the velocity reduction is constrained by the event-pairs that span the mainshock, stations recording fewer type A event-pairs have larger standard errors. The velocity decrease in the 1–5 Hz frequency band is around -0.25% , which agrees well with the velocity drop in shallow layers (< 2 km) revealed by ambient noise cross-correlations (Wu et al., 2016). At depths greater than 2 km, velocity drop estimated from noise correlation in Wu et al. (2016) also matches well with our results in the 10–20 Hz frequency band. It is worth noting that the conclusion in Wu et al. (2016) is based on the assumption of correlation coda composed entirely of surface waves. These agreements suggest earthquake coda at 1–5 Hz is sensitive to velocity perturbation near the Earth’s surface while the 10–20 Hz coda is more sensitive to changes at depth. We also observe a positive correlation between the coseismic velocity drop and the earthquake strong motion for the 1–5 Hz result; however, at 10–20 Hz, except for a few stations with large standard errors, velocity reduction does not vary with PGV. We hypothesize that this is because high-frequency coda is composed of waves scattered throughout the volume of the crust, which results in a much smaller velocity change signature. This interpretation implies earthquake coda of different wavelengths have different origins. In Figure 3, we note that shortly after the S wave, there is a sequence of low-frequency arrivals, which last much longer than the rapidly decaying high-frequency component. The arrival of these low-frequency waves coincides with the onset of the time-shift discrepancy. We hypothesize that the apparent velocity change observed at low frequency is a result of these long-duration vibrations, which implies that understanding the composition of these long-period coda waves is central to interpreting the observed velocity variations.

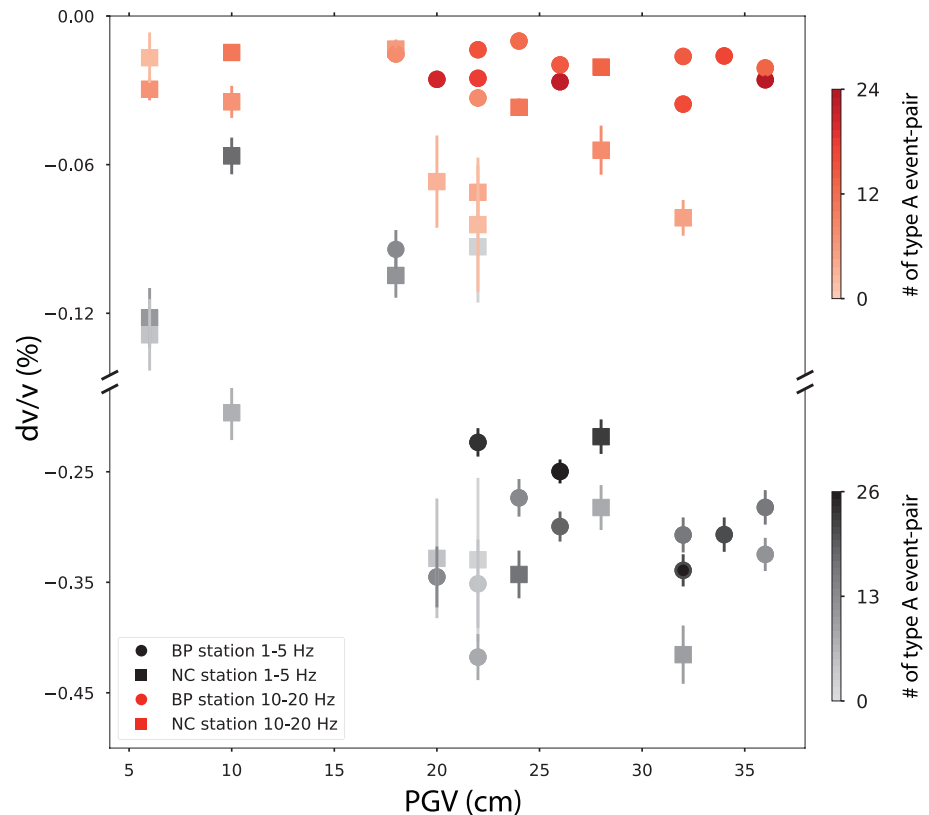


Figure 7. Correlation between PGV and estimated coseismic velocity reduction. Error bars show standard error and color indicates the number of type A event-pairs included in each estimate. The fewer type A event-pairs leads to larger standard errors. PGV, peak ground velocity.

5. Origin of Long-Period Coda

Previous studies (e.g., Ben-Zion & Malin, 1991; Ellsworth & Malin, 2011; Li et al., 1997) reported that fault zones can act as a waveguide and trap seismic waves due to the large impedance contrast with the surrounding crust. Li et al. (2006, 2007) used fault-zone guided waves (FZGW) to delineate the velocity change in the earthquake damage zone at Parkfield. FZGW are evanescent waves and become negligible on stations away from the fault (Li et al., 1990). Because most of our stations are well outside of the fault zone and the velocity change estimated for stations inside or close to the fault zone (e.g. BP.EADB and BP.MMNB) do not exhibit a significant difference from other stations, FZGW do not appear to strongly affect the observed low-frequency coda. Other than the FZGW, there are many studies examining the composition of the coda. Some favor the hypothesis that earthquake coda is generated by scattering off structure near the surface. Levander and Hill (1985) demonstrated through numerical simulations that body waves could be converted to long-duration trapped surface waves in the presence of a shallow low-velocity layer. Dodge and Beroza (1997) used the source array technique to analyze the low-frequency coda of local events near the rupture sites of the 1989 Loma Prieta and the 1984 Morgan Hill earthquakes, and found that the arrivals throughout the 26 s-long coda window are strongly clustered in azimuth and takeoff angle, implying the coda consists primarily of waves scattered near the station. Sleep (2009) studied changes in the S-P delay of repeating earthquakes near Parkfield and separated the coda into a direct coda contribution from depth and a reverberating coda contribution from near the surface. Here we present independent, direct observations to support the near-surface coda generation mechanism.

We study seismic records acquired at different depths at SAFOD. The SAFOD Pilot Hole Seismic Array included 32 three-component geophones equally spaced from 850 to 2,100 m depth (Chavarria et al., 2004). In the same well, a downhole distributed acoustic sensing (DAS) array covers depths from the surface to 800 m. The detailed description of the SAFOD experiment can be found in Zoback et al. (2011) and the

Table 2
Deep earthquakes recorded at San Andreas fault observatory at depth

| Seismic array | Date | Time | Latitude | Longitude | Depth | Mag (M_d) |
|---------------|---------------|-------------|----------|------------|--------|---------------|
| Geophone | May 25, 2003 | 19:32:57.25 | 35.96833 | −120.51850 | 10.605 | 2.39 |
| DAS | June 30, 2017 | 15:05:13.00 | 35.96833 | −120.52417 | 10.750 | 2.46 |

Abbreviation: DAS, distributed acoustic sensing.

description of the DAS array can be found in Lellouch et al. (2019). Unfortunately, these two experiments do not overlap in time; however, in the Double-Difference catalog, we find two deep events beneath the SAFOD well that are very close in space. One of them is recorded by the geophone array and the other by the DAS array. The details of these two earthquakes are listed in Table 2. Lellouch et al. (2019) estimated the seismic velocity in the top 800 m using the DAS records. We follow their work and compute the velocity at depth using the geophone waveforms with a first-break picking algorithm. The integrated velocity profiles, along with those derived from near-surface chemical explosions (regenerated from Pollitz et al., 2012) are shown in Figure 8a. The surface chemical sources suffer from strong decay and are hard to analyze at depth, especially for S-waves, which are much weaker due to the source mechanism. A low velocity zone that can trap seismic energy and lead to long-duration coda waves, is clearly observed in the shallow layers. Catchings et al. (2002) conducted a 5 km long high-resolution seismic imaging survey across the San Andreas fault zone and the SAFOD site. Their P-wave velocity model is in very good agreement with ours, although it lacks high spatial resolution. Given the lack of clear reflectors in the shallow section, surface seismic surveys are limited in their ability to retrieve gradual changes in the velocity profile. Nonetheless, their model is yet another confirmation of the near-surface low-velocity structure in the study area.

Figure 8b shows the seismic wavefields in three frequency bands, 1–5, 10–20, and 40–50 Hz. To account for using different earthquakes and for the different instrument responses, in each frequency band we normalize the DAS recordings by the average peak S amplitude of the channels in the deepest 40 m and normalize the geophone signals by the peak S amplitude recorded at the shallowest level. By doing so, we constrain the waveforms on the shallowest geophone and the deepest DAS channels to share similar S-wave energy. The wavefields from these two events align surprisingly well, but the high-frequency and low-frequency content behaves very differently with depth. Specifically, we observe a clear energy decay from deep to shallow layers, especially in the 40–50 Hz frequency band; at both 1–5 and 10–20 Hz, energy amplification is clearly observed in the shallow low-velocity zone. More importantly, for the 1–5 Hz frequency band, the wavefields are dominated by the energy concentrated near the surface; DAS channels, especially in the top 200 m, record remarkably sustained coda energy. These observations match well with the simulations in Levander and Hill (1985) and support our hypothesis that the low-velocity shallow layers trap low-frequency seismic waves. The absence of the high-frequency reverberation is possibly due to the strong scattering and attenuation (Blakeslee et al., 1989). This implies that the high-frequency energy present in the coda is scattered throughout the volume of the crust.

To reinforce the argument that the earthquake coda is dominated by the near-surface reverberations, we present the analysis of the coda wave interferometry between the co-located stations BP.VCAB and NC.PVC. We select local earthquakes larger than magnitude 1.5 since the year 2008 from the Double-Difference catalog. We manually check all the seismograms and exclude those with strong noise or other events appearing within 1 min after the earthquake origin time. We vary the starting time of the coda wave from two to six times the S-wave travel-time and compare the responses from different coda segments. Each coda window lasts 6 s. We apply one-bit normalization and perform cross-coherence, with station BP.VCAB as the virtual source, to obtain the correlation functions. The results are bandpass-filtered between 1 and 20 Hz and shown in Figure 9. We observe stable and consistent phases obtained from both early and late coda. In all cases, these correlation functions peak at 0.2 s, corresponding to a velocity of 1 km/s, given the 200 m depth interval between the two stations. This velocity matches well with our S-wave velocity model in the shallowest layers, suggesting a dominant wave propagating upwards from station BP.VCAB to station NC.PVC at the S-wave speed. We also observe a weaker but coherent arrival on the negative time lag, at the same 0.2 s time interval. This phase originates from waves propagating downwards, from station NC.PVC to

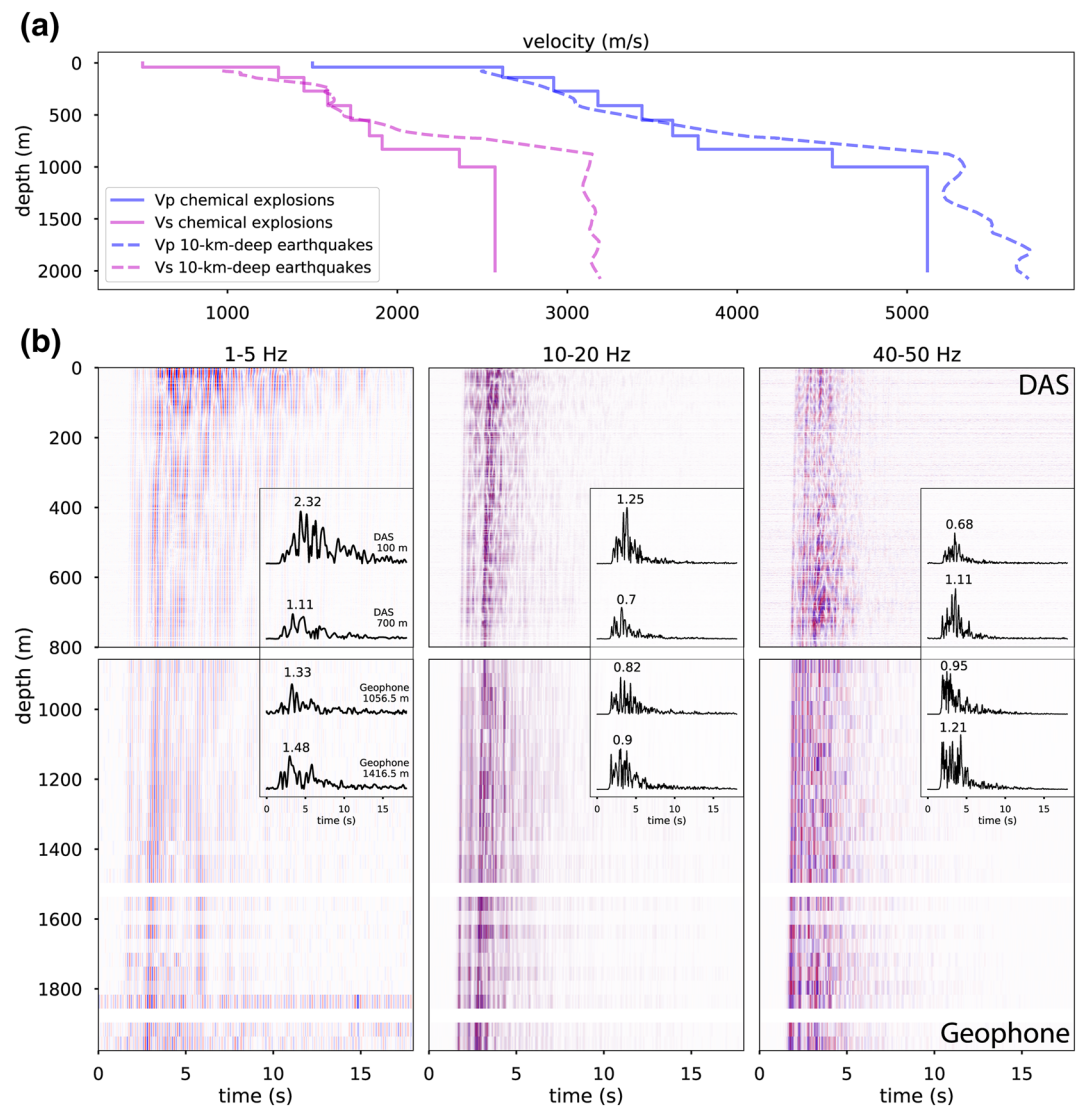


Figure 8. Seismic observations at SAFOD. (a) Velocity profile with depth. Solid lines show the P- and S-wave velocities inferred from two deep earthquakes listed in Table 1. The dashed lines are velocities derived from near-surface chemical explosions at the same site. (b) Seismic waveforms for three frequency bands recorded on downhole DAS (top) and deep geophone arrays (bottom). The inset in each panel shows envelopes of seismograms sampled at several depths. Relative amplitudes in each frequency band are preserved and the number on top of each trace indicates the maximum amplitude. SAFOD, San Andreas fault observatory at depth; DAS, distributed acoustic sensing.

station BP.VCAB. The other arrivals at larger time lags possibly correspond to reflected waves due to deep interfaces. The fact that we observe upgoing and downgoing waves on both the early and late coda confirms our hypothesis on coda wave reverberating in shallow layers.

Our velocity change analysis reveals that low-frequency coda reflects a significantly larger coseismic velocity drop compared to the high-frequency coda. This further suggests that the velocity change is shallow, with low-frequency waves strongly sampling a shallow velocity perturbation. The nonmonotonic time shift in the 5–10 Hz frequency band also favors such an interpretation, as the near-surface reverberation gradually attenuated along the coda, the estimated time shift first increases then decreases, reflecting the sensitivity of the velocity change shifting from the shallow sediments to the deep crust. We did not find repeating earthquakes during the very brief operation period of the DAS array. It is not straightforward to place stronger constraints on the depth extent of the velocity change based on our observations. Figure S6 demonstrates

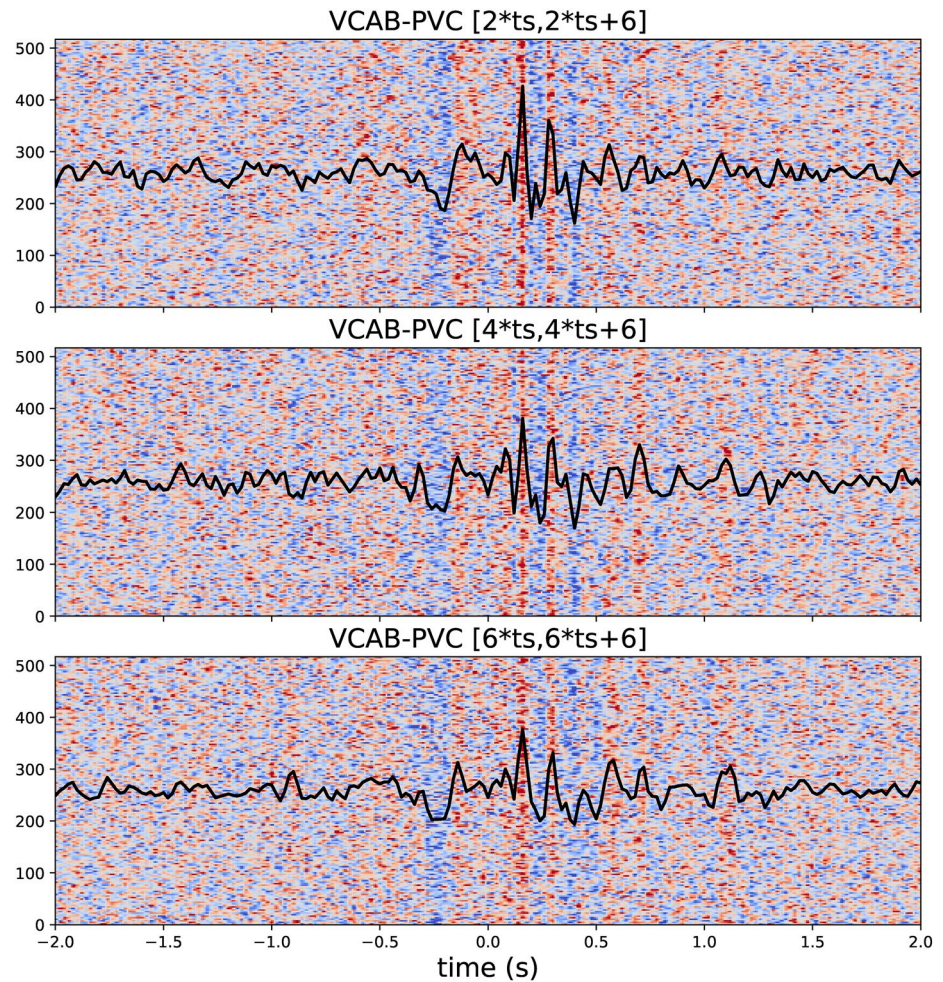


Figure 9. Earthquake coda wave interferometry between co-located stations BP.VCAB and NC.PVC. Each panel shows the result using different coda segments, indicated by the panel title. The background displays the correlation functions from all earthquakes considered and the black curve gives their average.

that the long-lasting coda seen in the near surface in the 1–5 Hz band is also observed at the bottom of the DAS array (800 m depth) but with much weaker energy. The sensitive range of the long-wavelength trapped wave may be confined by the depth of the sedimentary rocks, which is about 1–2 km in the study area (Hole et al., 2006), with very low velocities in the upper 100 m (Catchings et al., 2002). This depth range of the sedimentary layer is consistent with the depth extent of the velocity decrease revealed by ambient noise results (Wu et al., 2016).

6. Discussion and Conclusion

We analyze the relative velocity change at Parkfield using repeating earthquakes. Our results reveal that velocity changes have a frequency-dependent response. The low-frequency change is more significant than that at high frequencies. Comparing with the depth profile of the velocity change analyzed through ambient noise in the same area (Wu et al., 2016), our low-frequency coseismic velocity drop agrees well with the shallow velocity change and the high-frequency result shows a good match with the change at depth. We also observe a positive correlation between seismic velocity drop and earthquake strong motion at low frequencies, but find no clear correlation for the high-frequency coda waves. These observations suggest the high-frequency coda is dominated by seismic energy from large depths while the low-frequency coda predominantly originate from shallow structures.

We provide new evidences to support the hypothesis that low-frequency coda waves are primarily reverberations that are strongly amplified in a low-velocity zone near the surface. This observation is supported by the velocity structure at SAFOD, provided by the downhole seismic arrays' high-resolution recordings of continuous wavefields. We apply coda wave interferometry on the co-located borehole and surface stations to further prove our hypothesis. The near-surface effect is reasonably expected yet rarely discussed in the composition of the coda of the noise cross-correlation. As shown in our study, the combination of frequency and time-lapse dependent analysis of travel-time changes in the coda is critical to unravel the depth extent of velocity changes. Therefore, it is important to model the partitioning between body and surface waves in the coda, as proposed in Obermann, Planès, Larose, Sens-Schönfelder, et al. (2013) and Obermann et al. (2019). However, their simulations did not include intrinsic attenuation, expected to be strong in unconsolidated or loose sediments, and did not incorporate a realistic velocity profile, which we find to be critical to our interpretation. Simulations with more realistic models, and the analysis of frequency dependent changes for other earthquakes, should help advance the understanding of the correlation coda, which has been widely used in real-time monitoring.

Given our interpretation of the earthquake coda wave and the frequency dependence we observe in the velocity change, we support the notion that the observed coseismic velocity drop is due to effects near the surface. Along with other studies, our results favor the interpretation that the velocity change is caused by coseismic material damage and postseismic healing at shallow depths due to dynamic stress perturbations caused by strong ground motion during large earthquakes.

Data Availability Statement

Geophone waveform data and metadata for this study were accessed through the Northern California Earthquake Data Center (NCEDC), <https://doi.org/10.7932/NCEDC>. The HRSN borehole data come from High Resolution Seismic Network, <https://doi.org/10.7932/HRSN>, operated by the UC Berkeley Seismological Laboratory, which is archived at the NCEDC. The DAS interrogator and recorded data have been supplied by OptaSense. Earthquake records can be accessed through <https://doi.org/10.5281/zenodo.3701838>. The PGV ShakeMap data are obtained from the Center for Engineering Strong Motion Data (CESMD).

Acknowledgments

The authors thank Kasper van Wijk, an anonymous reviewer and editor Rachel Abercrombie for their valuable comments and suggestions.

References

- Beaucé, E., Frank, W. B., & Romanenko, A. (2018). Fast matched filter (FMF): An efficient seismic matched-filter search for both CPU and GPU architectures. *Seismological Research Letters*, 89(1), 165–172.
- Ben-Zion, Y., & Malin, P. (1991). San Andreas fault zone head waves near Parkfield, California. *Science*, 251(5001), 1592–1594.
- Beroza, G. C., Cole, A. T., & Ellsworth, W. L. (1995). Stability of coda wave attenuation during the Loma Prieta, California, earthquake sequence. *Journal of Geophysical Research*, 100(B3), 3977–3987.
- Blakeslee, S., Malin, P., & Alvarez, M. (1989). Fault-zone attenuation of high-frequency seismic waves. *Geophysical Research Letters*, 16(11), 1321–1324.
- Boatwright, J., Bundock, H., Luetgert, J., Seekins, L., Gee, L., & Lombard, P. (2003). The dependence of PGA and PGV on distance and magnitude inferred from Northern California Shakemap data. *Bulletin of the Seismological Society of America*, 93(5), 2043–2055.
- Brenguier, F., Campillo, M., Hadziioannou, C., Shapiro, N. M., Nadeau, R. M., & Larose, E. (2008). Postseismic relaxation along the San Andreas fault at Parkfield from continuous seismological observations. *Science*, 321(5895), 1478–1481.
- Brenguier, F., Shapiro, N. M., Campillo, M., Ferrazzini, V., Duputel, Z., Coutant, O., & Nercessian, A. (2008). Toward forecasting volcanic eruptions using seismic noise. *Nature Geoscience*, 1(2), 126.
- Catchings, R., Rymer, M., Goldman, M., Hole, J., Huggins, R., & Lippus, C. (2002). High-resolution seismic velocities and shallow structure of the San Andreas fault zone at middle mountain, Parkfield, California. *Bulletin of the Seismological Society of America*, 92(6), 2493–2503.
- Chavarria, J. A., Malin, P. E., & Shalev, E. (2004). The SAFOD pilot hole seismic array: Wave propagation effects as a function of sensor depth and source location. *Geophysical Research Letters*, 31(12), L12S07. <https://doi.org/10.1029/2003GL019382>
- Clements, T., & Denolle, M. A. (2018). Tracking groundwater levels using the ambient seismic field. *Geophysical Research Letters*, 45(13), 6459–6465. <https://doi.org/10.1029/2018GL077706>
- Dodge, D. A., & Beroza, G. C. (1997). Source array analysis of coda waves near the 1989 Loma Prieta, California, mainshock: Implications for the mechanism of coseismic velocity changes. *Journal of Geophysical Research*, 102(B11), 24437–24458.
- Ellsworth, W. L., & Malin, P. E. (2011). Deep rock damage in the San Andreas fault revealed by p- and s-type fault-zone-guided waves. *Geological Society London Special Publications*, 359(1), 39–53.
- Froment, B., Campillo, M., Chen, J., & Liu, Q. (2013). Deformation at depth associated with the 12 May 2008 MW 7.9 Wenchuan earthquake from seismic ambient noise monitoring. *Geophysical Research Letters*, 40(1), 78–82. <https://doi.org/10.1029/2012GL053995>
- Hadziioannou, C., Larose, E., Baig, A., Roux, P., & Campillo, M. (2011). Improving temporal resolution in ambient noise monitoring of seismic wave speed. *Journal of Geophysical Research*, 116(B7), B07304. <https://doi.org/10.1029/2011JB008200>
- Hale, D. (2013). Dynamic warping of seismic images. *Geophysics*, 78(2), S105–S115.
- Hole, J., Ryberg, T., Fuis, G., Bleibinhaus, F., & Sharma, A. (2006). Structure of the San Andreas fault zone at SAFOD from a seismic refraction survey. *Geophysical Research Letters*, 33(7), L07312. <https://doi.org/10.1029/2005GL025194>

- Hotovec-Ellis, A. J., Gomberg, J., Vidale, J., & Creager, K. C. (2014). A continuous record of intereruption velocity change at Mount St. Helens from coda wave interferometry. *Journal of Geophysical Research: Solid Earth*, *119*(3), 2199–2214. <https://doi.org/10.1002/2013JB010742>
- Lellouch, A., Yuan, S., Spica, Z., Biondi, B., & Ellsworth, W. (2019). Seismic velocity estimation using passive downhole distributed acoustic sensing records: Examples from the San Andreas fault observatory at depth. *Journal of Geophysical Research*, *124*(7), 6931–6948. <https://doi.org/10.1029/2019JB017533>
- Levander, A. R., & Hill, N. (1985). P-SV resonances in irregular low-velocity surface layers. *Bulletin of the Seismological Society of America*, *75*(3), 847–864.
- Li, Y.-G., Chen, P., Cochran, E. S., & Vidale, J. E. (2007). Seismic velocity variations on the San Andreas fault caused by the 2004 M6 Parkfield earthquake and their implications. *Earth Planets and Space*, *59*(1), 21–31.
- Li, Y.-G., Chen, P., Cochran, E. S., Vidale, J. E., & Burdette, T. (2006). Seismic evidence for rock damage and healing on the San Andreas fault associated with the 2004 M 6.0 Parkfield earthquake. *Bulletin of the Seismological Society of America*, *96*(4B), S349–S363.
- Li, Y.-G., Ellsworth, W. L., Thurber, C. H., Malin, P. E., & Aki, K. (1997). Fault-zone guided waves from explosions in the San Andreas Fault at Parkfield and Cienega Valley, California. *Bulletin of the Seismological Society of America*, *87*(1), 210–221.
- Li, Y.-G., Leary, P., Aki, K., & Malin, P. (1990). Seismic trapped modes in the Oroville and San Andreas Fault zones. *Science*, *249*(4970), 763–766.
- Matthews, M. V., & Segall, P. (1993). Estimation of depth-dependent fault slip from measured surface deformation with application to the 1906 San Francisco earthquake. *Journal of Geophysical Research*, *98*(B7), 12153–12163.
- Mikesell, T. D., Malcolm, A. E., Yang, D., & Haney, M. M. (2015). A comparison of methods to estimate seismic phase delays: Numerical examples for coda wave interferometry. *Geophysical Journal International*, *202*(1), 347–360.
- Murray, J., & Langbein, J. (2006). Slip on the San Andreas Fault at Parkfield, California, over two earthquake cycles, and the implications for seismic hazard. *Bulletin of the Seismological Society of America*, *96*(4B), S283–S303.
- Obermann, A., Planès, T., Larose, E., & Campillo, M. (2013). Imaging preeruptive and coeruptive structural and mechanical changes of a volcano with ambient seismic noise. *Journal of Geophysical Research*, *118*(12), 6285–6294. <https://doi.org/10.1002/2013JB010399>
- Obermann, A., Planès, T., Larose, E., & Campillo, M. (2019). 4-D imaging of subsurface changes with coda waves: Numerical studies of 3-D combined sensitivity kernels and applications to the Mw 7.9, 2008 Wenchuan earthquake. *Pure and Applied Geophysics*, *176*(3), 1243–1254.
- Obermann, A., Planès, T., Larose, E., Sens-Schönfelder, C., & Campillo, M. (2013). Depth sensitivity of seismic coda waves to velocity perturbations in an elastic heterogeneous medium. *Geophysical Journal International*, *194*(1), 372–382.
- Peng, Z., & Ben-Zion, Y. (2006). Temporal changes of shallow seismic velocity around the Karadere-Düzce branch of the North Anatolian Fault and strong ground motion. *Pure and Applied Geophysics*, *163*(2), 567–600.
- Pollitz, F. F., Rubinstein, J., & Ellsworth, W. (2012). Source characterization of near-surface chemical explosions at SAFOD. *Bulletin of the Seismological Society of America*, *102*(4), 1348–1360.
- Poupinet, G., Ellsworth, W., & Frechet, J. (1984). Monitoring velocity variations in the crust using earthquake doublets: An application to the Calaveras Fault, California. *Journal of Geophysical Research*, *89*(B7), 5719–5731.
- Rubinstein, J. L., & Beroza, G. C. (2005). Depth constraints on nonlinear strong ground motion from the 2004 Parkfield earthquake. *Geophysical Research Letters*, *32*(14), L14313. <https://doi.org/10.1029/2005GL023189>
- Schaff, D. P., & Beroza, G. C. (2004). Coseismic and postseismic velocity changes measured by repeating earthquakes. *Journal of Geophysical Research*, *109*, B10302. <https://doi.org/10.1029/2004JB003011>
- Sens-Schönfelder, C., & Wegler, U. (2006). Passive image interferometry and seasonal variations of seismic velocities at Merapi Volcano, Indonesia. *Geophysical Research Letters*, *33*(21), L21302. <https://doi.org/10.1029/2006GL027797>
- Sheng, Y., Nakata, N., & Beroza, G. C. (2018). On the nature of higher-order ambient seismic field correlations. *Journal of Geophysical Research: Solid Earth*, *123*(9), 7969–7982. <https://doi.org/10.1029/2018JB015937>
- Sleep, N. H. (2009). Depth of rock damage from strong seismic ground motions near the 2004 Parkfield mainshock. *Bulletin of the Seismological Society of America*, *99*(5), 3067–3076.
- Waldhauser, F. (2001). hypoDD—A program to compute double-difference hypocenter locations (hypoDD version 1.0–03/2001). *US Geol. Surv. Open File Rep.*, *01*, 113.
- Waldhauser, F. (2009). Near-real-time double-difference event location using long-term seismic archives, with application to Northern California. *Bulletin of the Seismological Society of America*, *99*(5), 2736–2748.
- Wu, C., Delorey, A., Brenguier, F., Hadziioannou, C., Daub, E. G., & Johnson, P. (2016). Constraining depth range of S wave velocity decrease after large earthquakes near Parkfield, California. *Geophysical Research Letters*, *43*(12), 6129–6136. <https://doi.org/10.1002/2016GL069145>
- Zhu, W., & Beroza, G. C. (2018). PhaseNet: A deep-neural-network-based seismic arrival-time picking method. *Geophysical Journal International*, *216*(1), 261–273.
- Zoback, M., Hickman, S., & Ellsworth, W. (2011). Scientific drilling into the San Andreas fault zone—An overview of SAFOD's first five years. *Scientific Drilling*, *11*(1), 14–28.